

Carrier Phase Shift Method of SPWM for Concurrent Wired and Wireless Power Transfer Systems

Enes Ayaz, Ogün Altun, and Ozan Keysan

Abstract—This paper presents an approach for concurrent power transfer to wired and wireless systems using just a single inverter. The approach utilizes a novel carrier phase-shift (CPS) method that independently controls the inverter output voltages at the fundamental and the switching frequencies. This proposed method can be a cost-effective solution to wireless power transfer (WPT) systems used in contactless slip rings (CSR), which transfer power to auxiliary loads such as sensors, radars, and IoT devices. There are two separate converters in conventional CSR systems: one is for the motor drive, and the other is for the WPT system. It is proposed that the switching harmonics of the motor drive can also be utilized to excite the WPT system while the low-frequency component can still be used to drive the motor. In order to control these independently, the CPS method is introduced. The proposed method is investigated analytically for sinusoidal-PWM (SPWM). Then, an experimental setup consisting of a 3-phase 3-wire GaN-based inverter and a 3-phase motor is built. Experimental results show that the WPT and motor systems are operated concurrently, and their powers are controlled independently. The experimental results are compared with theoretical calculations to validate the proposed method, and they are in good agreement below 4% error.

Index Terms—Wireless power transfer, inductive power transfer, motor drive, concurrent power transfer, dual-band power transfer, carrier phase shift.

LIST OF ABBREVIATIONS

ω_{rl}	Lower resonant frequency of WPT. [rad/sec].
ω	Operation frequency of WPT. [rad/sec].
ω_c	Carrier frequency. [rad/sec].
ω_{rh}	Higher resonant frequency of WPT. [rad/sec].
ω_r	Resonant frequency of WPT. [rad/sec].
$\phi_{c(A,B,C)}$	Carrier phases [°].
ϕ_{CPS}	The amount of carrier phase shift. (°)
ϕ_o	Fundamental phases [°].
A_{INV}	Inverter line-to-line voltage gain to DC-link.
A_{WPT}	WPT AC-AC voltage gain.
C_{Rx}	Rx capacitance [F].
C_{Tx}	Tx capacitance [F].
CV	Constant voltage.
f_o	Fundamental frequency [Hz].
f_s	Switching frequency [Hz].
f_{sh}	Higher sideband ($f_s - 2f_o$) [Hz].
f_{sl}	Lower sideband ($f_s - 2f_o$) [Hz].
J_k	k th order Bessel function.
J_o	Zeroth order Bessel function.

k	Coupling factor.
L_{Rx}	Rx inductance [H].
L_{Tx}	Tx inductance [H].
M	Mutual inductance [H].
m_a	Modulation index.
P_{rated}	Output power of WPT system [W].
Q_{RX}	Quality factor of receiver side including load.
R_L	Load resistance [Ω].
S	Switching function.
V_{DC}	DC-link voltage [V].
V_D	Equivalent centered harmonic drive (input) voltage of WPT system [V_{RMS}].
V_{OUT}	Output voltage of WPT system [V_{RMS}].
$V_{sh}(m_a)$	Line-to-line voltage at the higher sideband frequency for modulation index [V_{RMS}].
$V_{sl}(m_a)_{RMS}$	Line-to-line voltage at the lower sideband frequency for modulation index [V_{RMS}].
$V_s(m_a)$	Line-to-line voltage at the switching frequency for modulation index [V_{RMS}].
Z_{RX}	Receiver side impedance of WPT [Ω].
Z_{TX}	Transmitter side impedance of WPT [Ω].

I. INTRODUCTION

Wireless power transfer (WPT) systems have been commonly used in many applications such as EV chargers [1], consumer electronics [2], wearable devices [3], and contactless slip rings [4]. They provide several advantages like operation under harsh environments, increased mobility, etc. Compared to other WPT methods such as capacitive power transfer (CPT), WPT in radio frequency (RF), and WPT in ultrasonic; inductive power transfer (IPT) is the most common technique, which provides a moderate transfer distance, high power, and better efficiency [5]. IPT systems are primarily composed of a high-frequency converter, a set of transmitter (Tx), and receiver (Rx) coils with compensation elements and rectifier circuits. The compensation circuits create a resonant structure that amplifies the frequencies near the resonant frequency and attenuates the other frequencies, which means that they provide a power transfer at a single frequency, although high-frequency converters generate a square wave with high order harmonics.

Multi-frequency operation rather than single frequency to increase the power of single-load [6] or transfer power concurrently to multiple loads [7]–[14] are studied in the literature. Thus, the number of switches decreases with the same VA

ratings, transmitted power increases, and the utilization rate of DC-link voltage increases. In [6], a single inverter is used with multi-resonant circuits amplifying the fundamental and the third harmonic of the square wave. The third harmonic component increases the transmitted power without increasing the VA rating of the semiconductor devices. However, it is not possible to independently regulate the third harmonic component in such a system. In [7], a dual-band WPT system is introduced to make Tx compatible with two different WPT standards. However, in these systems two separate sets of coils and drivers are used, allowing design flexibility but increasing system complexity and cost. In [8], a single-inverter-based dual-frequency WPT system is proposed using the programmed PWM method. The system can regulate the output voltage for multiple receivers. The programmed PWM provides that one WPT frequency is equal to the effective switching frequency, which reduces the switching losses. Nevertheless, the programmed PWM is computationally complex since it requires switching angle calculation using offline algorithms. Hence, such a method is not feasible in dynamic systems. In [10], multi-frequencies are achieved by comparing superimposed sinusoidal reference signals with the high-frequency triangular carrier signals. In addition, a phase shift can be given between the superimposed reference signals to increase the utilization rate of the DC-link voltage [11]. However, in these methods, the switching frequency is higher than the operating frequencies of the WPT system, which increases the switching losses.

Apart from the aforementioned studies, multi-frequency systems can also be implemented to combine wireless and wired power transfer concurrently since they could co-exist in dynamic applications [15], [16]. One of these applications is a contactless slip ring (CSR) used in many areas, such as the field excitation of wound rotor synchronous motor, radar systems, robotic arms, and IoT devices [17]–[19]. In conventional CSR systems, an inverter is readily available to drive the actuator, and the power transfer to moving frames is granted via a WPT system, consisting of a high-frequency converter and a set of Tx-Rx coils.

In this study, a motor and an auxiliary system are driven concurrently by a single converter as shown in Fig. 1.a. It is proposed that the already existing inverter of the drive can be used as a multi-frequency inverter; thus, the high-frequency converter of the WPT system can be eliminated, reducing the cost and complexity. Since the power of WPT is smaller than the motor, the motor drive can be used without increasing VA ratings. Conventional motor drives use several modulation techniques (such as SPWM, SVPWM, DPWM) to adjust the speed and torque of the motor. However, independent control of the WPT system cannot be achieved only using these techniques. Therefore, the carrier phase shift (CPS) method is proposed, which provides independent control of the dual-band output voltage.

The rest of the paper is organized as follows. Section II presents the modulation methods and the proposed CPS method. Section III delivers the design stage of the WPT system. Section IV gives experimental results to validate the theoretical calculations. Section IV compares the proposed system

with existing studies in the literature. Section V discusses the implementation of the proposed system to conventional industrial drives.

II. SYSTEM PROPOSAL AND MODULATION METHOD

A 3-phase 3-wire (3Φ -3W) motor and a WPT system for auxiliary rotating loads are driven by a single inverter with sinusoidal pulse width modulation (SPWM) as a proof-of-concept. The circuit diagram of the system and the expected voltage and current waveforms are shown in Fig. 1.b. In this section, firstly, the analytical modeling of applied SPWM will be investigated. Secondly, the carrier phase shift (CPS) method is proposed, and the effect of this method on the magnitude of the dual-band output will be argued. Finally, the equivalent centered harmonic approach to control the amount of CPS is presented.

A. Analytical analysis of SPWM

SPWM is established by comparing a high-frequency triangular carrier signal and a fundamental (modulating) signal. This fundamental signal is the reference signal of the motor, and the operating frequency of WPT is cultivated using the first harmonic of the carrier signal. The analytical model of SPWM can be obtained as given in (1), using double Fourier analysis.

$$S = \frac{1}{2} + \frac{m_a}{2} \cos(\omega_o t + \theta_o) + \frac{2}{\pi} \sum_{i=1}^{\infty} J_o\left(i\frac{\pi}{2}m_a\right) \sin\left(i\frac{\pi}{2}\right) \cos\left(i(\omega_c t + \theta_c)\right) + \frac{2}{\pi} \sum_{i=1}^{\infty} \sum_{k=-\infty}^{\infty} \left(\begin{array}{c} \frac{1}{i} J_k\left(i\frac{\pi}{2}m_a\right) \sin\left((i+k)\frac{\pi}{2}\right) \\ \cos\left(i(\omega_c t + \theta_c) + k(\omega_o t + \theta_o)\right) \end{array} \right) \quad (1)$$

There are four main components for each leg: DC, fundamental, switching harmonics, and sidebands. The switching harmonics and their sidebands cannot be adjusted independently, and they change along with the modulation index, which is used to control the magnitude of the fundamental frequency.

TABLE I
THE SEQUENCES OF FUNDAMENTAL FREQUENCIES, SWITCHING, AND ITS SIDEBAND HARMONICS FOR INVERTER LEGS.

Frequency	Leg A	Leg B	Leg C	Sequence
f_o	0°	120°	-120°	Positive
$f_s - 2f_o$	0°	120°	-120°	Positive
f_s	0°	0°	0°	Zero
$f_s + 2f_o$	0°	-120°	120°	Negative

Moreover, the phases of these components vary for each leg of the inverter, and they have positive, negative, or zero sequences, as shown in Table II-A. The normalized line-to-line voltage harmonics are given in Fig. 3. Since the switching harmonic is zero-sequence, it is eliminated in a line-to-line connection, which means that the line-to-line connected WPT system is excited only by the sideband components. Additionally, the magnitude of these sideband components cannot be

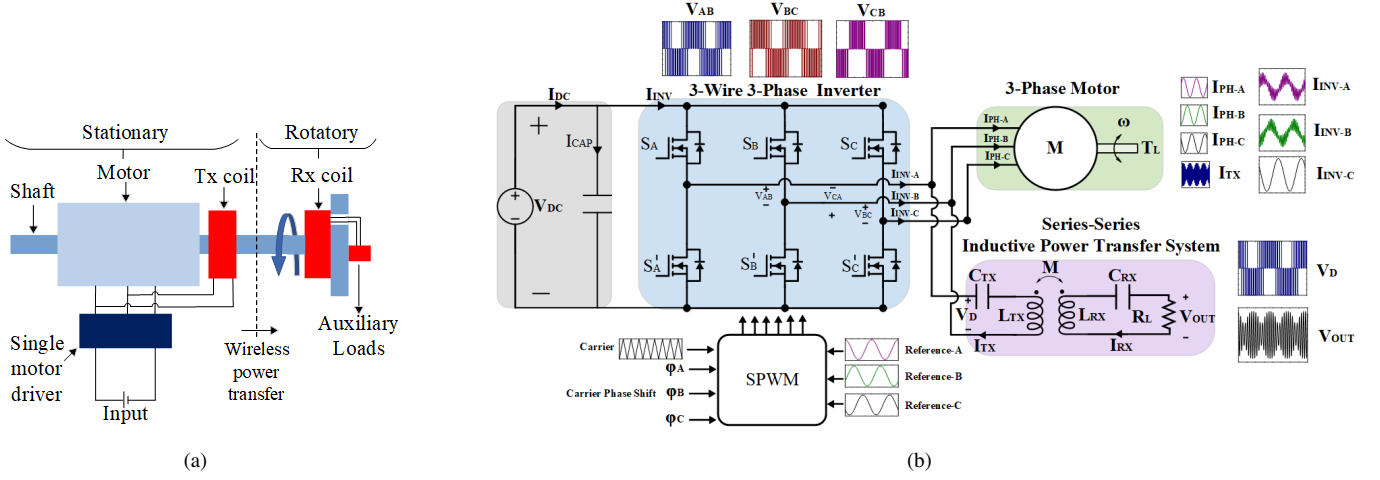


Fig. 1. a) The proposed single-inverter multi-frequency motor drive and WPT system to energize IoT devices or sensors on the rotating frames. b) The circuit diagram of a single inverter system, which drives concurrently 3W-3 Φ motor and WPT system.

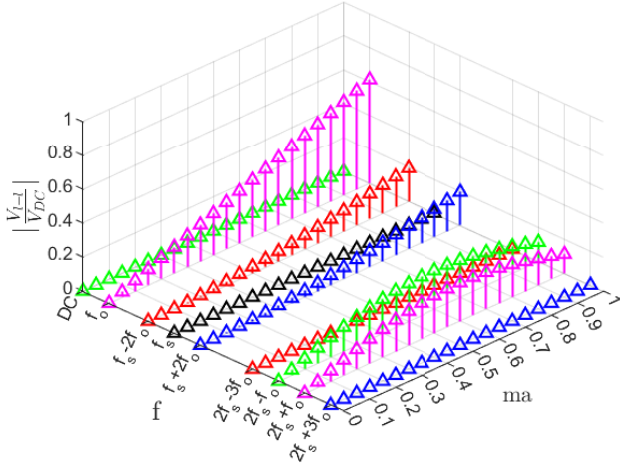


Fig. 3. The harmonic distribution of a line-to-line voltage among different modulation indices without carrier phase shift.

controlled independently. Therefore, in order to regulate the WPT power, a DC-DC converter can be added to the receiver

for post-regulation, which increases cost and complexity, or frequency detuning can be applied, worsening the power factor and hence efficiency. However, these regulation methods cannot guarantee to transfer of power under each modulation index (m_a) since sideband components converge to zero as m_a comes up to zero. In other words, the transferred power of the WPT system is decreasing while m_a is nearing zero. This diminished power is undesirable since the auxiliary loads may require the rated power for each operating condition of the motor.

B. The Proposed Carrier Phase Shift (CPS) Method

Normally, the power transmitted to the WPT system cannot controlled independently for every m_a value due to the non-controllable magnitude of sidebands and the disappearance of the switching frequency in the line-to-line connection. It is proposed that these problems can be solved by giving a phase shift between carrier signals of two legs. As can be seen from the double Fourier analysis in (1), phases of switching frequency and its sidebands change as a function of the phase of the carrier signal. In this study, for the coherency, the WPT system will be connected between legs A and B, and a carrier phase shift will be given to leg B, as given in (2).

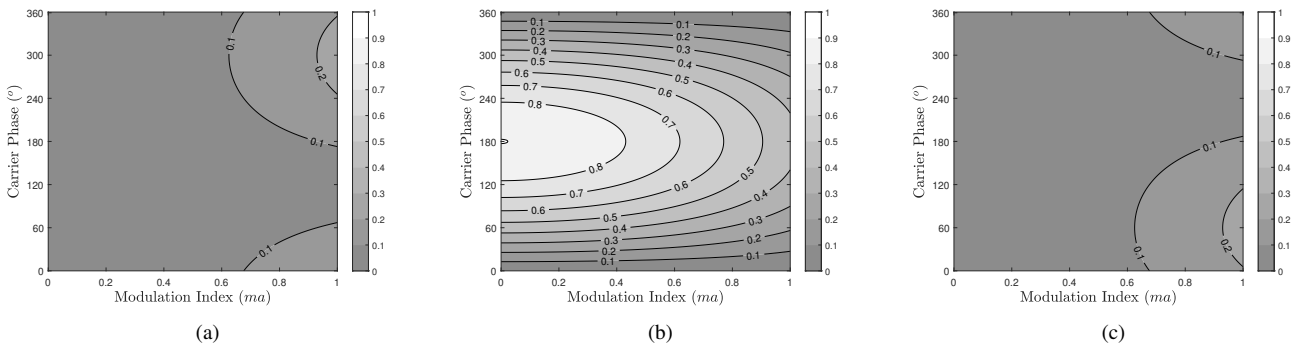


Fig. 2. Normalized inverter output voltages $|V_{l-l}|/V_{DC}$. (a) Lower sideband of the switching frequency (f_{sl}). (b) Switching frequency (f_s). (c) Higher sideband of the switching frequency (f_{sh}).

$$\text{Carrier phases} \begin{cases} \phi_{cA} = 0 \\ \phi_{cB} = \phi_{CPS} \\ \phi_{cC} = 0 \end{cases} \quad (2)$$

The magnitudes of switching frequency and sideband harmonics vary as given in (3, 4, 5). Therefore, we can adjust the magnitude of each component by giving a carrier phase shift.

$$V_{sl}(m_a) = \frac{2}{\pi} J_2 \left(m_a \frac{\pi}{2} \right) \sqrt{1 - \cos(\phi_{CPS} + 120^\circ)} \quad (3)$$

$$V_s(m_a) = \frac{2}{\pi} J_0 \left(m_a \frac{\pi}{2} \right) \sqrt{1 - \cos(\phi_{CPS})} \quad (4)$$

$$V_{sh}(m_a) = \frac{2}{\pi} J_2 \left(m_a \frac{\pi}{2} \right) \sqrt{1 - \cos(\phi_{CPS} - 120^\circ)} \quad (5)$$

The magnitudes can be calculated for variable carrier phase shifts and modulation indices, as shown in Fig. 2. The key voltage and current waveforms are given in Fig. 4 with introduced CPS. While the fundamental signal is determined by modulating signals, the switching frequency and its sidebands are controlled by CPS.

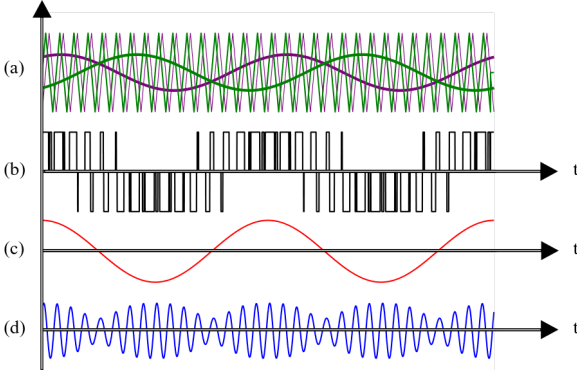


Fig. 4. Key Waveforms. (a) Ph-A (purple) and Ph-B (green) carrier triangles and sinusoidal references. (b) Line-to-line voltage of ph-A and ph-B (V_{AB}). (c) The waveform of fundamental frequency of (V_{AB}). (d) The waveform of the switching frequency and its sidebands of (V_{AB}).

A challenge is to determine the amount of the phase shift, which must guarantee a constant power transfer for any modulation indices. As shown in Fig. 2, while the magnitude of the switching frequency harmonic increases by increasing CPS, the magnitude of the sidebands decreases. Therefore, a combined equivalent magnitude value is required to select the range of phase shift.

C. Equivalent centered harmonics approach

Considering the quality factor of WPT systems, the gain of the switching frequency and its sideband harmonics are nearly equal since their frequencies are close enough. Instead of investigating each component in the time domain, we can build an equivalent drive voltage assuming all components to have the same frequency. The RMS equivalent drive voltage (V_D) can be calculated using (6) since all these frequencies are orthogonal to each other.

$$V_D = \sqrt{V_{sl}^2 + V_{sw}^2 + V_{sh}^2} \quad (6)$$

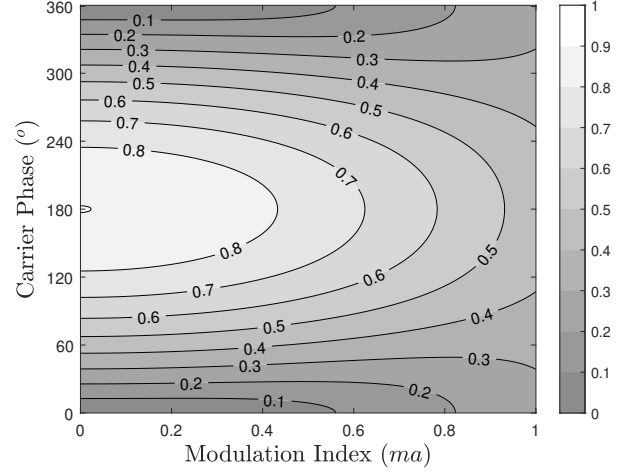


Fig. 5. Normalized inverter output voltages $|V_{l-l}|/V_{DC}$ using the center harmonic approach.

Using the equivalent center harmonic approach, a normalized drive voltage is shown for various carrier phase shifts and modulation indices in Fig. 5. As can be seen, for each modulation index, we can guarantee the normalized gain between 0.25 and 0.45 by keeping the carrier phase shift between 30° and 60° . While the carrier phase shift is approaching 180° , the normalized drive voltage increases. However, at this point, we cannot fully control the voltage level; for example, the drive voltage acquired at $m_a = 0$ cannot be reached at $m_a = 1$.

III. WPT SYSTEM PARAMETERS SPECIFICATION

A WPT system is established as a proof of concept. The input-output specifications of these system are given in Table II. The effective drive voltage is selected as 0.3 times V_{DC} , which means that the input voltage of WPT is kept constant at $30 V_{RMS}$.

TABLE II
THE INPUT-OUTPUT SPECIFICATIONS OF THE WPT SYSTEM

Ratings	
DC-link Voltage (V_{DC})	100 V
WPT Input Voltage (V_D)	30 V_{RMS}
Output Voltage (V_{OUT})	15 V_{RMS}
Rated Power (P_{rated})	24 W

The system is series-series (SS) compensated, the circuit diagram of which is shown in Fig. 6, and the operating frequency is selected between 80 kHz and 90 kHz.

In general, auxiliary systems such as sensors and IoT devices have varying loads, and it is desired to achieve constant voltage (CV) output for any load conditions. Thus, the WPT system is designed to supply CV output in this study. For SS compensation, the frequency of the load-independent voltage is different from the resonant frequency (ω_r), and there are two

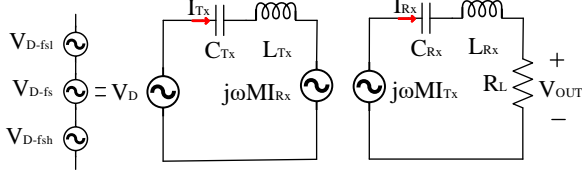


Fig. 6. The first harmonic approach circuit diagram of the WPT system.

operating frequencies (ω_{rl} , ω_{rh}) that satisfies load independent output voltage. The output voltage (V_{OUT}) and voltage gain (A_{WPT}) of the SS compensated system are given in (7) and (8).

$$\begin{aligned} V_{OUT} &= \frac{j\omega M I_{Tx} R_L}{Z_{Rx}} \\ &= \frac{j\omega M}{Z_{Rx}} \left(\frac{V_{IN}}{\frac{\omega^2 M^2}{Z_{Rx}} + Z_{Tx}} \right) R_L \end{aligned} \quad (7)$$

$$\begin{aligned} &= \frac{j\omega M V_{IN}}{\omega^2 M^2 + Z_{Tx} Z_{Rx}} R_L \\ A_{WPT} &= \left| \frac{V_{OUT}}{V_{IN}} \right| \\ &= \frac{\omega M}{\omega^2 M^2 + Z_{Tx} Z_{Rx}} R_L \end{aligned} \quad (8)$$

In order to calculate the frequencies providing load-independent voltage gain, the differential equation of $\frac{dA_{WPT}}{dR_L} = 0$ should be solved [20]. The load-independent voltage operating frequencies are found as in (9) according to selected coupling factor (k) and angular resonant frequency ω_r .

$$\begin{aligned} \omega_{rl} &= \omega_r \sqrt{\frac{1}{1+k}} \\ \omega_{rh} &= \omega_r \sqrt{\frac{1}{1-k}} \end{aligned} \quad (9)$$

The minimum load resistance that delivers the rated power can be calculated as in (10).

$$R_L = \frac{V_{OUT}^2}{P_{rated}} \quad (10)$$

Receiver inductance is calculated using the load resistance, operating frequency that is selected as ω_{rh} , and the chosen quality factor of Rx (Q_{Rx}) as provided in (11).

$$\begin{aligned} Q_{Rx} &= \frac{\omega_{rh} L_{Rx}}{R_L} \\ L_{Rx} &= \frac{Q_{Rx} R_L}{\omega_{rh}} \end{aligned} \quad (11)$$

The voltage gain of WPT should be 0.5 to achieve the desired output voltage of 15 V_{RMS} . The load-independent voltage gain is presented in (12), and the Tx inductance is found using (13).

$$A_{WPT(\omega_{rh})} = \left| \sqrt{\frac{L_{Rx}}{L_{Tx}}} \right| \quad (12)$$

$$L_{Tx} = \frac{L_{Rx}}{A_{WPT(\omega_{rh})}^2} \quad (13)$$

Then, the mutual inductance is calculated as in (14).

$$M = k \sqrt{L_{Tx} L_{Rx}} \quad (14)$$

Finally, the compensation capacitances are adjusted as in (15).

$$\begin{aligned} C_{Tx} &= \frac{1}{\omega_r^2 L_{Tx}} \\ C_{Rx} &= \frac{1}{\omega_r^2 L_{Rx}} \end{aligned} \quad (15)$$

The initial parameters and the derived parameters are given in Table III. The voltage gain-frequency graphs of the designed WPT system for different load resistances are shown in Fig. 7.

TABLE III
WPT SYSTEM PARAMETERS

Initial/Chosen Parameters	Values	Derived Parameters	Values
P_{rated}	24 W	A_{WPT}	0.5
V_D	30 V_{RMS}	R_L	9.3 Ω
V_{out}	15 V_{RMS}	L_{Rx}	50 μH
f_{rh}	85 kHz	L_{Tx}	200 μH
Q_{Rx}	2.9	M	40 μH
k	0.4	f_r	65.85 kHz
		C_{Tx}	29.2 nF
		C_{Rx}	117 nF

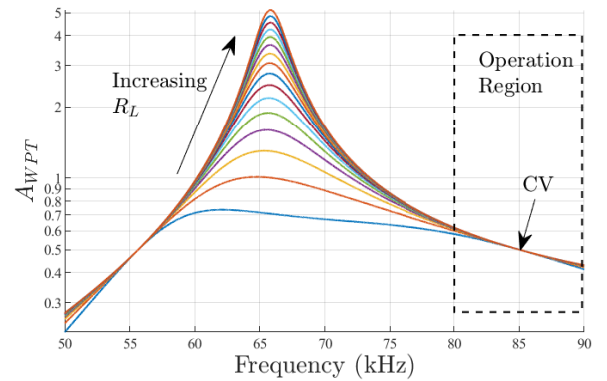


Fig. 7. The voltage gain of WPT system for different load resistances.

IV. EXPERIMENTAL VALIDATION

An experimental setup is established consisting of a GaN-based 3 Φ -3W inverter and an AC motor to validate the proposed method. The experimental setup is shown in Fig. 8. The AC motor is loaded using a DC generator, and the WPT system is connected to its shaft.

A. Multi-frequency Inverter Test

In this part, the inverter is driven by the SPWM modulation technique with and without the proposed CPS method. Thus, the variation in the magnitudes of the fundamental frequency, switching frequency, and its sidebands are investigated.

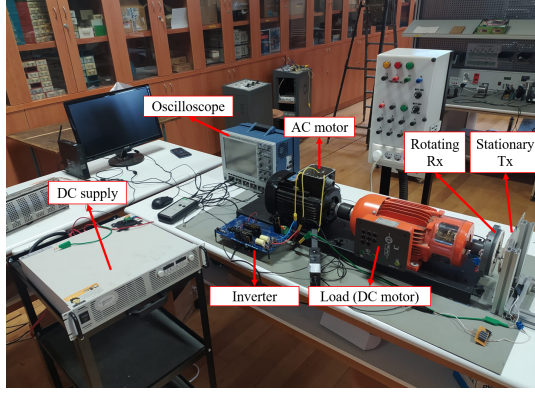


Fig. 8. Experimental Setup.

The inverter output voltages are shown in Fig. 9 for the phase shift of $\phi_B = 0^\circ$ and $\phi_B = 47.5^\circ$. The harmonic distributions of the normalized inverter output voltage are compared in Table V for analytical and experimental results, which have a good agreement with an error band of less than 10%. It can be observed that the carrier phase shift method controls the magnitude of the switching frequency component and its sidebands while the magnitude of the fundamental component stays constant.

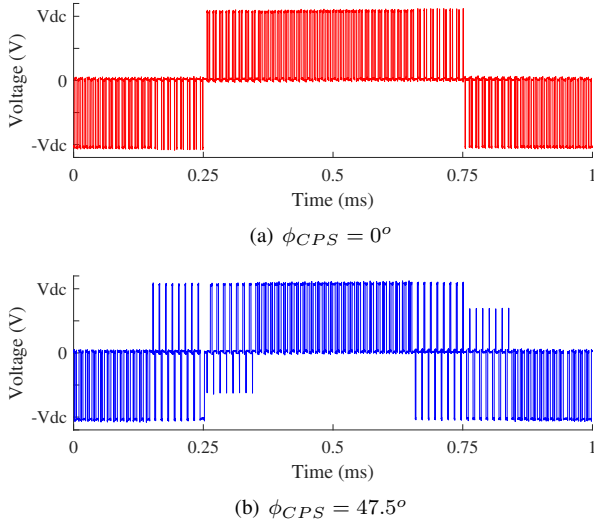


Fig. 9. Inverter output voltage (V_{l-l}) (or called as drive voltage V_D) at $m_a = 0.6$ for $\phi_{CPS} = 0^\circ$ and $\phi_{CPS} = 47.5^\circ$

TABLE V
THEORETICAL AND EXPERIMENTAL RESULTS OF INVERTER OUTPUT HARMONIC DISTRIBUTION FOR $\phi_{CPS} = 0^\circ$ AND $\phi_{CPS} = 47.5^\circ$

		$A_{INV} (\hat{V}_U/V_{dc})$			
		at f_o	at f_1	at f_s	at f_h
$m_a = 0.6$ $\phi_{CPS} = 0^\circ$	Theoretical	0.519	0.113	0	0.113
	Experimental	0.532	0.110	0.011	0.115
	Error	2.5%	2.6%	-	1.7%
$m_a = 0.6$ $\phi_{CPS} = 47.5^\circ$	Theoretical	0.519	0.130	0.405	0.077
	Experimental	0.537	0.127	0.414	0.084
	Error	3.4%	2.3%	2.2%	9.1%

B. Concurrent Operation of motor and WPT

Carrier phase shift is adjusted to 40° with $m_a = 0.8$. First, the WPT system and the motor are driven individually and then concurrently. Fig. 10. shows the motor-only operation, and the motor current is ~ 1.75 A. Then, only the WPT system is connected, and it draws ~ 0.35 A. Finally, the inverter drives the motor and WPT system concurrently, and it is observed that the systems draw almost the same current for the identical modulation index and carrier phase shift.

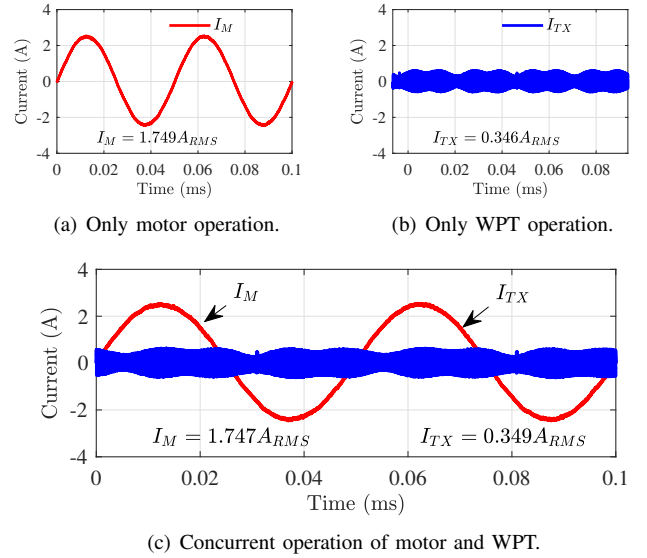


Fig. 10. Motor and IPT currents.

C. WPT Power Control

The power of WPT systems changes along with the modulation indices if a constant carrier phase shift is employed. In order to keep the WPT power constant, a variable carrier phase shift should be applied. The normalized power was

TABLE IV
CARRIER PHASE SHIFT REQUIREMENTS FOR DIFFERENT MODULATION INDEX.

Modulation index (m_a)	0	0.1	0.2	0.3	0.4	0.5	0.6	0.7	0.8	0.9	1
Phase shift (θ_{an}) (Theoretical)	41	41	41.2	42.4	44.1	46.0	48.2	50.3	51.9	52.0	46
Phase shift (θ_{exp}) (Experimental)	41	41.2	41.8	42.7	44	45.7	47.5	49	50	51	46
Error $ \frac{\theta_{an} - \theta_{exp}}{\theta_{an}} 100\%$	0%	0.5%	1.4%	0.7%	0.2%	0.6%	1.4%	2.5%	3.6%	1.92%	0%

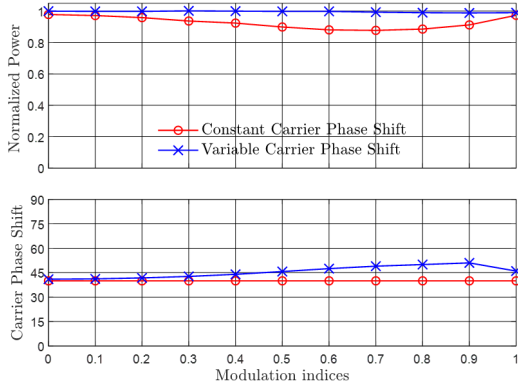


Fig. 11. Powers of the WPT system for constant and variable carrier phase shift.

experimentally obtained for constant and variable phase shifts, which are shown in Fig. 11. In the modulation indices where normalized power reduces, the carrier phase shift is increased to compensate for the diminished power. Phase shift values used in the experimental setup to keep constant power are also compared with theoretical calculations in Table IV, and the error stays below 4%.

D. Transients of Motor and WPT on Load Changes

In this part, the effect of the load changes on the WPT system and motor is investigated. Firstly, the mechanical load of the AC motor is varied, while other parameters such as switching frequency and modulation index are kept constant. It is observed that the WPT system is not disturbed by the load changes, as shown in Fig 12.a. Then, the load of the WPT system is altered using the same procedure. As expected, currents of the AC motor do not change, as shown in Fig. 12.b. Unless the modulation index or switching frequency changes, a system's load changes do not affect the operation of the other system.

V. COMPARISON WITH EXISTING STUDIES

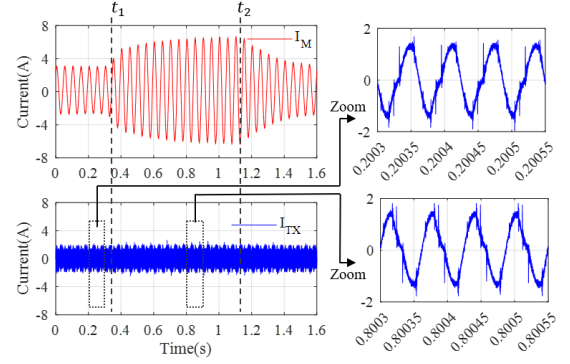
Existing multi-frequency WPT systems in the literature are given in Table VI. The proposed method provides independent control of the dual-band output voltage. Unlike [8], it is not required offline calculations where it is not possible to apply dynamic applications like motor drive systems. In addition, the operating frequency of the WPT system is matched with the switching frequency compared to [10], [11]. If WPT operates at the modulated frequency rather than the switching frequency, the switching losses increase to achieve the same coil sizes. Thus, directly utilizing the switching frequency is significant to make the system feasible. Furthermore, a single converter is presented rather than using two separate converters as in [7], which helps to reduce the system cost and complexity.

VI. DISCUSSION

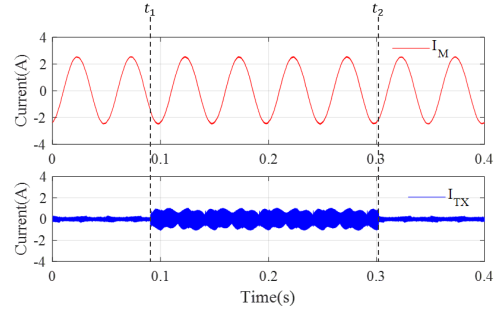
In this section, the feasibility of implementing the proposed system on conventional industrial motor drives is discussed.

A. Wide-bandgap Semiconductors based Motor Drives

The operating frequency of WPT systems has a direct impact on their size; the higher frequency is the smaller coil [21]. The switching frequency of conventional motor



(a) At t_1 , the motor load torque is increased, and at t_2 , the motor load torque returns to the former value.



(b) At t_1 , The WPT load resistance is decreased, and at t_2 , WPT load resistance returns to the former value.

Fig. 12. Transient load changes. a) Motor load changes. b) IPT load changes.

TABLE VI
COMPARISON WITH EXISTING STUDIES IN THE LITERATURE.

	Transfer Channels	Converter Numbers (Tx)	Offline Algorithm	Operating Frequency
[6]	1	1	Not Required	$\geq f_s$
[7]	2	2	Not Required	f_s
[8]	2	1	Required	$\leq f_s$
[11]	4	1	Not Required	$< f_s$
This work	2	1	Not Required	$= f_s$

drives has traditionally been around 20 kHz due to the switching losses of silicon (Si)-based transistors [22]. IPT systems are not feasible in this frequency range since the Tx-Rx coils get bulky. However, with recent advancements in semiconductor technology, higher switching frequencies (up to several hundred kHz) can be achieved with wide-bandgap semiconductors such as silicon carbide (SiC) or gallium nitride (GaN) based motor drives without sacrificing efficiency [23], [24]. These advancements make the proposed method feasible, and it is considered that just an algorithm update would be enough to implement it.

B. Current Modulation Techniques of Conventional Drives

Many modulation techniques such as Sinusoidal PWM (SPWM), Space Vector PWM (SVPWM), and Discontinuous PWM (DPWM) are used in industrial motor drives. Each modulation technique has its advantages. For example, while SVPWM effectively utilizes the DC link voltage, DPWM provides reduced switching losses. Although the proposed system is implemented with SPWM, it can also be applied with other modulation techniques. The change in the magnitude of

the switching frequency over modulation indices is presented in Fig. 13 for SPWM and SVPWM. It is observed that the tendency of the magnitude of the switching harmonic of SVPWM is similar to SPWM, and it can be controlled in line-to-line connection via the proposed CPS as presented before.

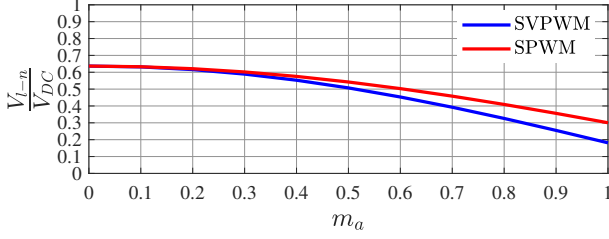


Fig. 13. The normalized inverter voltage ($\frac{V_{l-n}}{V_{DC}}$) of the switching harmonics over modulation indexes (m_a)

VII. CONCLUSION

This paper proposes a concurrent dual-frequency power transfer method for wired and wireless systems using just a single inverter. The proposed method can reduce the system cost and size for applications that require power transfer to rotating frames, such as rotating sensors, radars, and auxiliary systems. This study also presents a novel carrier phase shift (CPS) method to regulate the power transferred to the WPT systems. Therefore, active converters on the Rx side are not required, which reduces the complexity and weight of the system on the rotating frame. The system can be implemented in conventional industrial motor drives, which are on the trend of passing wide-bandgap semiconductors that enable higher switching frequencies. Thus, a sweet operating frequency is achieved considering the switching losses and the size of the WPT system. In order to validate the proposed system, an experimental setup with a GaN-based drive was established. It was acquired that the switching harmonic and the fundamental frequency is controlled independently by the proposed CPS method. It was observed that the experimental results are coherent with analytical calculations.

REFERENCES

- [1] H. Chen, Z. Qian, R. Zhang, Z. Zhang, J. Wu, H. Ma, and X. He, "Modular four-channel 50 kw wpt system with decoupled coil design for fast ev charging," *IEEE Access*, vol. 9, pp. 136 083–136 093, 2021.
- [2] Y. Zhang, S. Chen, X. Li, and Y. Tang, "Design methodology of free-positioning nonoverlapping wireless charging for consumer electronics based on antiparallel windings," *IEEE Transactions on Industrial Electronics*, vol. 69, no. 1, pp. 825–834, 2022.
- [3] S. H. Kang, J. H. Choi, F. J. Harackiewicz, and C. W. Jung, "Magnetic resonant three-coil wpt system between off/in-body for remote energy harvest," *IEEE Microwave and Wireless Components Letters*, vol. 26, no. 9, pp. 741–743, 2016.
- [4] X. Zhu, L. Liu, and H. Qi, "Performances of a contactless energy transfer system for rotary ultrasonic machining applications," *IEEE Access*, vol. 8, pp. 51 981–51 990, 2020.
- [5] M. Etemadrezai, "22 - wireless power transfer," in *Power Electronics Handbook (Fourth Edition)*, fourth edition ed., M. H. Rashid, Ed. Butterworth-Heinemann, 2018, pp. 711–722. [Online]. Available: <https://www.sciencedirect.com/science/article/pii/B9780128114070000246>
- [6] Z. Pantic, K. Lee, and S. M. Lukic, "Multifrequency inductive power transfer," *IEEE Transactions on Power Electronics*, vol. 29, no. 11, pp. 5995–6005, 2014.
- [7] D. Ahn and P. P. Mercier, "Wireless power transfer with concurrent 200-khz and 6.78-mhz operation in a single-transmitter device," *IEEE Transactions on Power Electronics*, vol. 31, no. 7, pp. 5018–5029, 2016.
- [8] C. Zhao and D. Costinett, "Gan-based dual-mode wireless power transfer using multifrequency programmed pulse width modulation," *IEEE Transactions on Industrial Electronics*, vol. 64, no. 11, pp. 9165–9176, 2017.
- [9] C. Qi, H. Miao, Z. Lang, and X. Chen, "A generalized methodology to generate, amplify and compensate multi-frequency power for a single-inverter-based mf-mr-s-wpt system," *IEEE Access*, vol. 8, pp. 181 513–181 525, 2020.
- [10] C. Xia, N. Wei, H. Zhang, S. Zhao, Z. Li, and Z. Liao, "Multifrequency and multiload mcr-wpt system using hybrid modulation waves spwm control method," *IEEE Transactions on Power Electronics*, vol. 36, no. 11, pp. 12 400–12 412, 2021.
- [11] J. Wu, L. Bie, W. Kong, P. Gao, and Y. Wang, "Multi-frequency multi-amplitude superposition modulation method with phase shift optimization for single inverter of wireless power transfer system," *IEEE Transactions on Circuits and Systems I: Regular Papers*, vol. 68, no. 5, pp. 2271–2279, 2021.
- [12] Y. Xiao, C. Liu, Y. Huang, and S. Liu, "Concurrent wireless power transfer to multiple receivers with additional resonant frequencies and reduced power switches," *IEEE Transactions on Industrial Electronics*, vol. 67, no. 11, pp. 9292–9301, 2020.
- [13] F. Liu, Y. Yang, Z. Ding, X. Chen, and R. M. Kennel, "A multifrequency superposition methodology to achieve high efficiency and targeted power distribution for a multiload mcr wpt system," *IEEE Transactions on Power Electronics*, vol. 33, no. 10, pp. 9005–9016, 2018.
- [14] W. Jin, A. T. L. Lee, S.-C. Tan, and S. Y. Hui, "A gallium nitride (gan)-based single-inductor multiple-output (simo) inverter with multi-frequency ac outputs," *IEEE Transactions on Power Electronics*, vol. 34, no. 11, pp. 10 856–10 873, 2019.
- [15] Y. Cao and J. A. A. Qahouq, "Analysis and evaluation of a dual-variable closed-loop control of power converter with wireless and nonwireless power transfer," *IEEE Transactions on Industrial Electronics*, vol. 66, no. 4, pp. 2668–2679, 2019.
- [16] Q. Deng, Y. Cheng, F. Chen, D. Czarkowski, M. K. Kazimierzuk, H. Zhou, and W. Hu, "Wired/wireless hybrid charging system for electrical vehicles with minimum rated power requirement for dc module," *IEEE Transactions on Vehicular Technology*, vol. 69, no. 10, pp. 10 889–10 898, 2020.
- [17] M. Maier and N. Parspour, "Operation of an electrical excited synchronous machine by contactless energy transfer to the rotor," *IEEE Transactions on Industry Applications*, vol. 54, no. 4, pp. 3217–3225, 2018.
- [18] K. D. Papastergiou and D. E. Macpherson, "An airborne radar power supply with contactless transfer of energy—part i: Rotating transformer," *IEEE Transactions on Industrial Electronics*, vol. 54, no. 5, pp. 2874–2884, 2007.
- [19] G. Lee and G. Ahn, "Wireless power transfer of daisy chain structure on rotating spindle," in *2020 IEEE Wireless Power Transfer Conference (WPTC)*, 2020, pp. 384–387.
- [20] W. Zhang, S.-C. Wong, C. K. Tse, and Q. Chen, "Analysis and comparison of secondary series- and parallel-compensated inductive power transfer systems operating for optimal efficiency and load-independent voltage-transfer ratio," *IEEE Transactions on Power Electronics*, vol. 29, no. 6, pp. 2979–2990, 2014.
- [21] V. Shevchenko, O. Husev, R. Strzelecki, B. Pakhaliuk, N. Poliakov, and N. Strzelecka, "Compensation topologies in ipt systems: Standards, requirements, classification, analysis, comparison and application," *IEEE Access*, vol. 7, pp. 120 559–120 580, 2019.
- [22] S. Tiwari, O. . Midtgård, and T. M. Undeland, "Sic mosfets for future motor drive applications," in *2016 18th European Conference on Power Electronics and Applications (EPE'16 ECCE Europe)*, 2016, pp. 1–10.
- [23] A. K. Morya, M. C. Gardner, B. Anvari, L. Liu, A. G. Yepes, J. Doval-Gandoy, and H. A. Toliyat, "Wide bandgap devices in ac electric drives: Opportunities and challenges," *IEEE Transactions on Transportation Electrification*, vol. 5, no. 1, pp. 3–20, 2019.
- [24] W. Lee, S. Li, D. Han, B. Sarlioglu, T. A. Minav, and M. Pietola, "A review of integrated motor drive and wide-bandgap power electronics for high-performance electro-hydrostatic actuators," *IEEE Transactions on Transportation Electrification*, vol. 4, no. 3, pp. 684–693, 2018.